Ocean Science
Discussions

Open Access

EGU

Norwegian Atlantic Slope Current along the Lofoten Escarpment

Ilker Fer[1], Anthony Bosse[1, 2], and Johannes Dugstad[1]

[1]Geophysical institute, University of Bergen, and Bjerknes Centre for Climate Research, Bergen, Norway
[2]Now at Aix-Marseille Université, Université de Toulon, CNRS/INSU, IRD, MIO, UM 110, Marseille, France

Correspondence: Ilker Fer (ilker.fer@uib.no)

Abstract. Observations from moored instruments are analyzed to describe the Norwegian Atlantic Slope Current at the Lofoten Escarpment. The data set covers a 14-month period from June 2016 to September 2017, and resolves the core of the current from 200 to 650 m depth, between the 650 m and 1500 m isobaths. The along-slope current, vertically averaged between 200 and 600 m depth has an annual cycle amplitude of $0.1 \, \mathrm{m \, s^{-1}}$ with strongest currents in winter, and a temporal average of 0.15

5   $\mathrm{m \, s^{-1}}$. Higher frequency variability is characterized by fluctuations that reach $0.8 \, \mathrm{m \, s^{-1}}$, lasting for 1 to 2 weeks, and extend as deep as 600 m. In contrast to observations in Svinøy, the slope current is not barotropic and varies strongly with depth (a shear of 0.05 to $0.1 \, \mathrm{m \, s^{-1}}$ per 100 m in all seasons). Within the limitations of the data, the average volume transport is estimated at 2.8 ± 1.8 Sv (1 Sv $= 10^6 \, \mathrm{m^3 \, s^{-1}}$), with summer and winter averages of 2.3 and 4.0 Sv, respectively. The largest transport is associated with the high temperature classes ($> 7°$C) in all seasons, with the largest values of both transport and temperature

10   in winter. Calculations of the barotropic and baroclinic conversion rates using the moorings are supplemented by results from a high resolution numerical model. While the conversion from mean to eddy kinetic energy (e.g. barotropic instability) is likely negligible over the Lofoten Escarpment, the baroclinic conversion from mean potential energy into eddy kinetic energy (e.g. baroclinic instability), can be substantial with volume-averaged values of $(1-2) \times 10^{-4} \, \mathrm{W \, m^{-3}}$.

1   Introduction

15   The relatively mild climate of Norway is largely attributed to the northern extension of the North Atlantic Drift, the Norwegian Atlantic Current that transports warm and saline water masses toward the Arctic Ocean (Seager et al., 2002; Rhines et al., 2008). These nutrient-rich warm waters contribute to support the entire food chain and sustain the productive waters around Norway (see e.g., Sundby (2000) for a discussion on recruitment of Atlantic cod stocks). The circulation pattern is organized in two main branches originating from the Iceland-Faroe and Faroe-Shetland channels (Orvik and Niiler, 2002) (Fig. 1a): the

20   Norwegian Atlantic Slope Current (the slope current hereinafter) and the Norwegian Atlantic Front Current (the front current hereinafter). The diverging isobaths of the Lofoten Basin in the Norwegian Sea guide the two branches. The slope current follows the shelf break along the Norwegian continental slope northward and continues into the Barents Sea and Fram Strait. The front current follows the 2000-m isobath, veers west at the flanks of Vøring Plateau and continues poleward along the Mohn Ridge (Orvik and Niiler, 2002; Bosse and Fer, 2019).

25   The front current is relatively poorly known, and is not addressed in this study. At the Svinøy section (63°N, about 300 km downstream of the Faroe-Shetland Channel), a baroclinic geostrophic transport estimate of the front current was 3.4 Sv (1
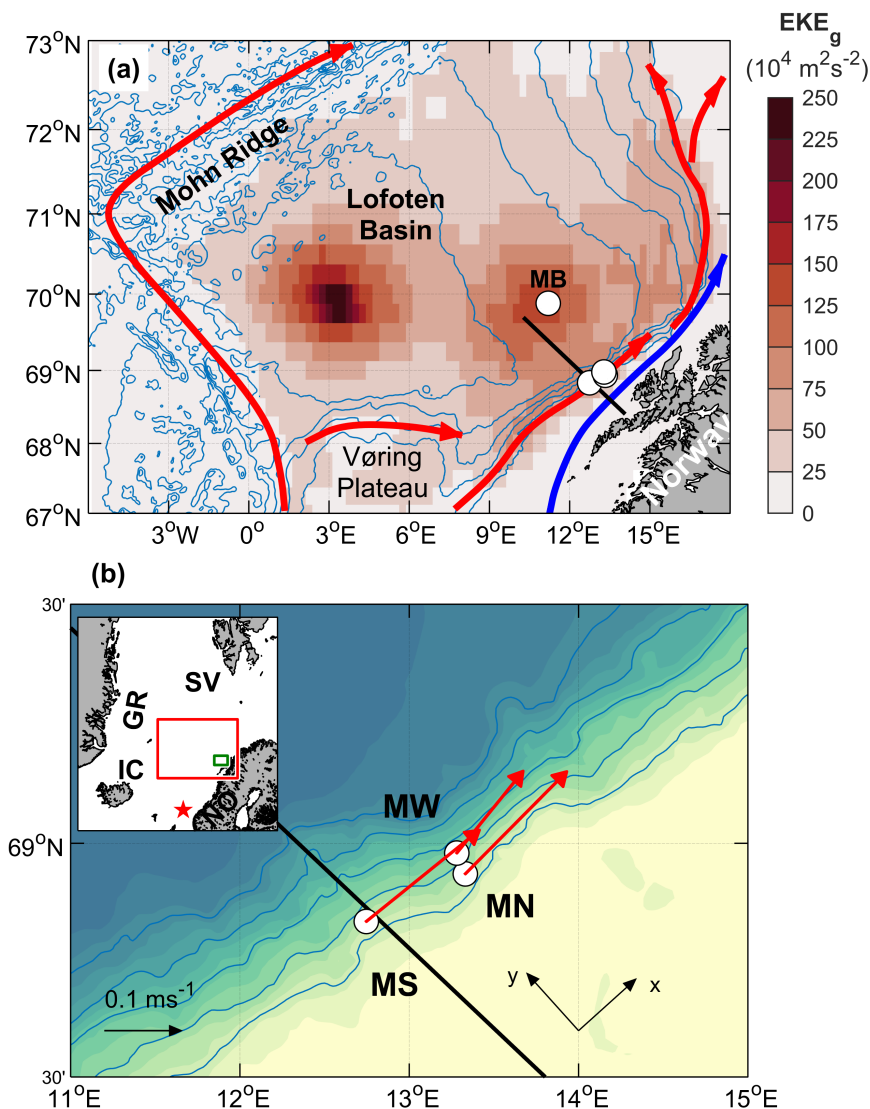
Figure 1. (a) Bathymetry of the Lofoten Basin in the Norwegian Sea (ETOPO1, contours at 500 m intervals) and the geostrophic EKE (EKE$_g$) from satellite altimeter observations, averaged over the period 1993 to 2018. General circulation of the warm Atlantic Water is indicated by red arrows showing the slope current and the front current. The Norwegian Coastal Current is indicated by the blue arrow. Black transect is the portion of Gimsøy section shown in Fig. 2. Mooring positions are shown by circles, also showing the basin mooring (MB) at the secondary EKE maximum. Lofoten Escarpment is the steep slope region near the slope moorings. (b) A zoom-in to the moorings analyzed in this study, showing MS, MN and MW together with 200–600 m depth-averaged current vectors (scale on lower left), Gimsøy section (black), and the orientation of the coordinate system (along-slope, x, and across-slope, y). Blue isobaths are drawn every 500 m. The inset is a location map with domains of (a) and (b) marked in red and green, respectively. The monitoring location for the Svinøy section is shown by the red star. NO: Norway, SV: Svalbard, IC: Iceland, GR: Greenland.

Sv $= 10^6$ m^3 s^{-1}) (Orvik et al., 2001); however, the total geostrophic transport from repeated Seaglider transects reached 6.8 Sv (Høydalsvik et al., 2013), implying a large barotropic contribution. Farther north, detailed glider observations of the front current over the Mohn Ridge confirm large transport rates giving 4.5 Sv annual average with approximately 2 Sv barotropic

30 contribution (Bosse and Fer, 2019).

University of Bergen, Norway, has monitored the slope current transport at the Svinøy section (star in the inset of Fig. 1b), south of the Vøring Plateau, with continuous measurements since 1995 (Orvik et al., 2001). The slope current there is about 40 km wide, between the 200 and 900 m isobaths, with an annual mean of 0.3 m s^{-1}. The average annual transport of this barotropic branch is 4.4 Sv (Orvik et al., 2001; Orvik and Skagseth, 2003). The slope current accelerates along steep topography

35 off the Lofoten Escarpment near the Lofoten Islands. The Norwegian Coastal Current (blue arrow Fig 1), carries relatively fresh water over the shelf and as the shelf gets narrow near the Lofoten Escarpment, there might interactions with the slope current. Here, there are no published moored current meter records, but surface drifters indicate velocities reaching 1 m s^{-1} (Andersson et al., 2011). The transport and variability of the slope current in this region is not known. It is hypothesized that the current becomes increasingly unstable near this topographic steepening. Using time-averaged fields of an eddy-resolving numerical

40 ocean simulation, Isachsen (2015) showed that the steep Lofoten Escarpment exhibits enhanced unstable baroclinic growth rates and large velocity variability, suggesting high lateral diffusion rates. The structure and transport of the slope current at the Lofoten Escarpment is the focus of this study.

The Lofoten Basin is affected by the Atlantic Water (AW) transport, and becomes a major heat reservoir that is exposed to large surface heat losses (Rossby et al., 2009b; Dugstad et al., 2019a) and substantial water mass transformations (Rossby et al.,

45 2009a; Bosse et al., 2018). The AW enters the basin both as a broad slab in the upper layers between the two branches (Rossby et al., 2009b; Dugstad et al., 2019a) and by eddies detached from the unstable slope current (Köhl, 2007; Isachsen, 2015; Volkov et al., 2015). The eddy-induced lateral heat fluxes distribute the heat in the basin (Spall, 2010; Isachsen et al., 2012; Dugstad et al., 2019a). The region is energized, manifested in the average geostrophic eddy kinetic energy (EKE$_g$, see Sect. 2) map showing two maxima (Fig. 1a): one in the center, associated with a permanent, energetic eddy (Ivanov and Korablev,

50 1995; Søiland and Rossby, 2013; Fer et al., 2018; Bosse et al., 2019), and a secondary maximum closer to the slope, likely associated with the variability induced by the slope current. The energetics and the variability of the slope current remain to be constrained by observations.

The study was conducted as a part of the "Water mass transformation processes and vortex dynamics in the Lofoten Basin of the Norwegian Sea" (PROVOLO) project. The overall objective of PROVOLO was to describe and quantify the processes and

55 pathways of energy transfer and mixing in the Lofoten Basin and their role in water mass transformation. Observations from multiple cruises, gliders and RAFOS floats were analyzed and reported elsewhere with focus on AW tranformation (Bosse et al., 2018), the permanent Lofoten Basin Eddy (Fer et al., 2018; Bosse et al., 2019) and the frontal structure across the Mohn Ridge (Bosse and Fer, 2019). The mooring component concentrated on the slope current. Here we report the first observations of the volume transport rates, energetics and their variability from weekly to seasonal time scales.

Table 1. Mooring deployment and recovery details. Total depth is estimated from the deepest pressure sensor, mooring line construction and the ship's echo sounder.

Mooring	Latitude	Longitude	Depth (m)	Deployed	Recovered
MS	68°N 50.038′	012°E 44.777′	672	31.05.2016	08.09.2017[a]
MN	68°N 56.109′	013°E 19.866′	655	01.06.2016	08.09.2017[b]
MW	68°N 58.759′	013°E 16.845′	1500	01.06.2016	08.09.2017
MB	69°N 52.89′	011°E 11.89′	2925	02.06.2016	09.09.2017

[a] Water column line is lost

[b] Water column line is recovered on 24.08.2016

2 Data

A set of 4 moorings was deployed across the continental slope of the eastern Lofoten Basin (Fig.1). A deployment and recovery summary is listed in Table 1, and full details are provided with the documentation following the data set (Fer, 2020). Mooring name convention is Mooring North (MN), South (MS), West (MW) and Basin (MB). MB was located at the secondary geostrophic EKE maximum (Fig. 1a) to address the mesoscale variability in the basin. Data from this mooring will be analysed for a separate study and are not reported here. The observations cover a 14-month period from June 2016 to September 2017.

The arrangement of the three moorings on the slope (Fig. 1b) was designed to cover the core of slope current (two moorings at the 650 m and 1500-m isobaths, MN and MW), and to investigate the co-variability along the slope (two moorings at the 650-m isobath). The along-slope distance between MS and MN is 26 km, and the cross-slope distance between MN and MW is about 6 km. Moorings MS and MN at the 650 m isobath each consisted of one bottom unit (approximately 25 m tall, with a RDI 75kHz Longranger acoustic Doppler current profiler (ADCP) in a spherical flotation and a Sea-Bird Scientific SBE37 Microcat), and a water column line with distributed conductivity-temperature-depth (CTD) sensors. This approach mitigated the high risk due to fisheries activities. The ADCP bottom unit and mooring line pairs were deployed close to each other at approximately the same isobath (within 5 m), and within 250 m horizontally, and will be treated as a single mooring. Unfortunately both water column mooring lines at MN and MS were damaged by fishing boats. The MS line was lost with no data return. The MN line was cut after 3 months. The drifting line together with the sensors were recovered, giving 3 (summer) months of temperature and salinity data in the water column. The current profile and the near-bottom CTD data from the bottom units were successfully recovered and cover the whole study period.

The moorings were densely instrumented and sampled at a hourly rate or faster, covering a large fraction of the water column. The instrument target depths can be seen on the vertical axis of Fig. 4, introduced later. Currents were measured using ADCPs, mainly RDI 75kHz Sentinel Workhorse for the moorings reported here, and point current meters (Anderaa SeaGuard). The ADCPs on MN, MS and MW were placed to cover the dynamic core of the slope current (at approximately 10 m height above seabed at the 650 m isobath, and at 740 m depth at the 1500 m isobath, each pointing upward with about 550 m range). Temperature, salinity and pressure were sampled using SBE temperature loggers (SBE56 and SBE39) and CTD

recorders (Microcat, SBE37). Detailed instrument distribution on moorings can be found in the data set documentation (Fer,
2020). Current measurements were corrected for magnetic declination. After all moorings were recovered, a calibration CTD
cast was made with all mooring SBE sensors attached to the ship's CTD frame. The temperature and salinity measurements
were corrected to be internally consistent, and also against the calibration cast and the profiles taken when the moorings were
in water. A data set was prepared after correcting for mooring knock downs caused by intense currents. The initial accuracy of
the SBE sensors are $\pm 2 \times 10^{-3}\,^\circ$C for temperature, $\pm 3 \times 10^{-4}$ S m^{-1} for conductivity, and ± 1 dbar for pressure (drift over
1 year is comparable to initial accuracy for temperature and pressure, and 10 times the initial accuracy for conductivity). For
the deployment setup used, the ADCPs have a single ping (profile) statistical error of 2.5 cm s^{-1}, which reduces to 0.4 cm s^{-1}
for the ensemble average profile with 35 pings. The compass direction is accurate to $\pm 2^\circ$. Conservative error estimates are ± 1
cm s^{-1} for velocity, $\pm 10^{-2}\,^\circ$C for temperature and $\pm 10^{-2}$ for practical salinity.

Hourly-averaged data set was filtered using a 14 day low-pass filter for background fields, and 35 h to 14 day band-pass filter
for eddy covariance and conversion rate calculations. In both cases a 3rd order Butterworth filter was used.

We rotated the coordinate system 42° from East, with x-axis pointing along-slope and y-axis cross-slope toward deeper water
(see Fig. 1b). Mean orientation of the slope was calculated using isobaths from ETOPO1 near the slope moorings. Current
components are along-slope, u, and across-slope, v. (In the figures, we explicitly use the notation u_a and u_x, respectively.)

Atmospheric forcing was obtained from ECMWF's ERA-Interim (Dee et al., 2011) reanalysis over the historical time period
from 1979 to 2018, and from higher resolution ERA-5 (C3S, 2017) reanalysis over the mooring observation period. Surface
net fluxes Q_{net} were computed from net shortwave and longwave contributions, as well as latent and sensible heat fluxes, as
$Q_{net} = Q_{sw} + Q_{lw} + Q_{sens} + Q_{lat}$, with downward heat fluxes defined to be positive. Time series of fluxes were extracted at
the nearest grid point from mooring sites. The geostrophic EKE (EKE$_g$) was obtained from the satellite altimeter observations
(product SEALEVEL_GLO_PHY_L4_REP_OBSERVATIONS_008_047), using the surface geostrophic velocities.

3   Context and environmental forcing

Hydrography data from the standard Gimsøy section were available from 4 occupations during the mooring period (on 30 Jul
2016, 19 Nov 2016, 8 Mar 2017 and 7 Jun 2017). An average section using the subset of stations taken in all 4 occupations,
is representative of the hydrography during the measurements (Fig. 2). The AW, identified by temperatures above 5° C and
absolute salinities $S_A > 35.17$, covered the 50–700 m layer from the shelf edge toward the basin, overlying the fresher and
colder Norwegian Sea Deep Water. The interface between these water masses meets the bottom slope at about 700 m. Relatively
fresh layer on the shelf is associated with the Norwegian coastal current. The moorings MN and MW, marked on Fig. 2, show
that the range of current measurements sufficiently covered the AW layer and the dynamical core at the slope identified by
sloping isotherms.

A summary of the environmental forcing during the measurement period shows that the net surface flux was typical of the
long-term average, with an event of strong heat loss exceeding 1 standard deviation (std) envelope from mid February to early
March (Fig. 3a). Wind speed showed a seasonal variability increasing from 5 m s^{-1} in summer to 12 m s^{-1} in winter (Fig. 3b).
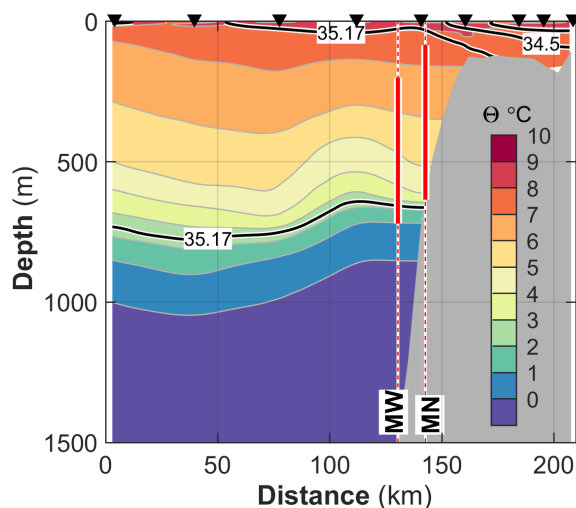
Figure 2. Conservative Temperature (Θ, in color, contours at 1°C interval) and Absolute Salinity (black lines, 34, 34.5 and 35.17 g kg^{-1} contours) distribution at Gimsøy section averaged over four occupations throughout the mooring period. Only stations (arrowheads) with four profiles are used. S$_A$ = 35.17 approximately corresponds to a practical salinity of 35 (typical value for AW) at this latitude, 300 dbar pressure and 5°C temperature. Bathymetry is from ETOPO1. The moorings MN and MW are shown at the distance on the section corresponding to the deployment isobaths. The vertical extent of the ADCP current profiling is marked with thick red.

We averaged the EKE$_g$ from satellite altimetry in a 30-km radius at the basin mooring location, MB (a EKE$_g$ maximum region, see Fig. 1a), and at MW (Fig. 3c). The EKE$_g$ records confirm that MB is 2 to 5 times more energetic in general, except in summer when both locations were relatively quiescent. In winter, the slope was as energetic as the basin.

4   Average properties and seasonal profiles

Profiles temporally averaged in the winter (DJF), spring (MAM), summer (JJA) and fall (SON) months at MW and MN show strong vertical shear in u_a in the upper 600 m at both moorings (Fig. 4). In contrast to the barotropic slope current at Svinøy, the current at the Lofoten Escarpment clearly has a strong baroclinic component. Background shear between 200 and 600 m depth was 0.05 to 0.10 m s^{-1} per 100 m in all seasons, with a maximum in the fall. The fall was characterized by maximum baroclinicity, whereas winter was characterized by maximum barotropic currents, consistent with increased winds. Increased baroclinicity in the fall could partly be due to seasonal freshening of the coastal current reinforcing the density gradients, and partly due to increased Ekman transport toward the shore observed from September to March (see northward winds implying eastward Ekman transport in Fig. 3b). It is also likely that the slope current could interact with the fresh coastal current due to the narrow shelf off the Lofoten Escarpment.

Over the full record, 200–600 m depth average u_a was 0.15 m s^{-1}. The strongest currents were observed in winter with an average of 0.20 m s^{-1} at MW and 0.25 m s^{-1} at MN (approximately twice the summer average) when the temperature
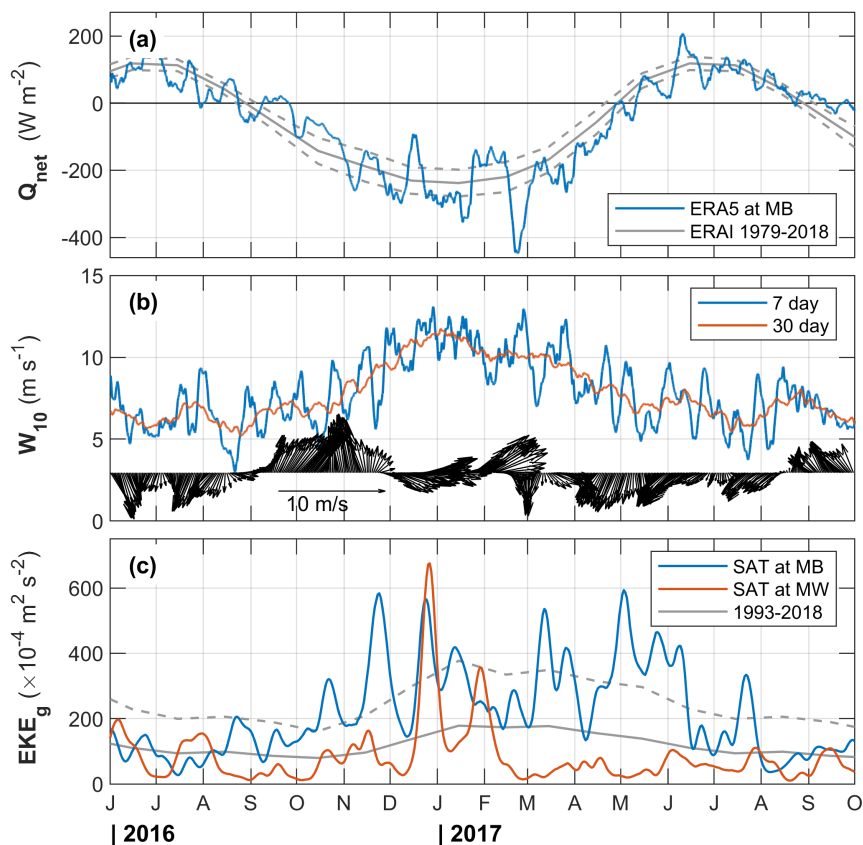
Ocean Science
Discussions

Open Access

Figure 3. Environmental forcing conditions throughout the mooring deployment period. a) Net surface heat flux, Q_{net} from ERA5 at the grid point closest to MB, together with monthly average and one standard deviation envelope for the period between 1979 and 2018. b) Weekly and monthly averages of 10-m wind speed and wind vectors from ERA5. c) EKE_g from satellite altimetry calculated at the grid point close to MB (blue) and MW (red), together with monthly average and one standard deviation between 1993 and 2018 at MB.

was also the largest. Average winter temperature at MW was 7.3°C, compared to 5.8°C (at MW) or 6°C (at MN) in summer. The average temperature in the 200–600 m range was warmer by more than 1°C in winter. This could partly be explained by the vertical redistribution by winter vertical mixing of heat contained in the seasonal thermocline, and partly by changes in AW properties flowing into the Nordic Seas. Cross-slope component was weak and approximately doubled in winter with an increased variability. In deep layers (>900 m) at MW, barotropic currents were between 0.05 and 0.10 m s^{-1}.
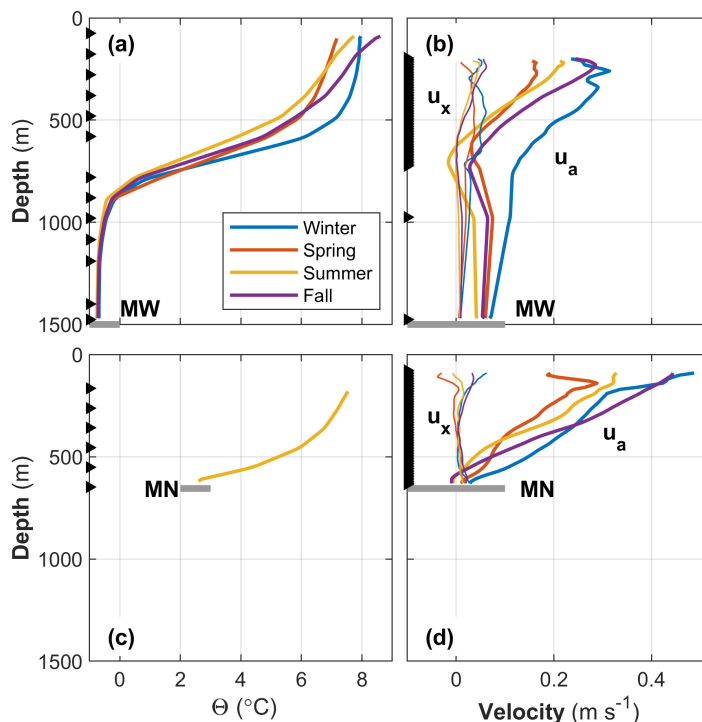
Ocean Science
Discussions

Open Access

EGU

Figure 4. Time averaged profiles of (a,c) Θ and (b,d) velocity components u_a (thick) and u_x (thin lines) for moorings MW (upper row) and MN (bottom row). Time averaging is made over seasons, winter, spring, summer and fall, as indicated in the legend. Gray horizontal line marks the sea bed. Arrowheads on the vertical axis mark the target depth of measurements.

5 Temporal variability

The currents measured at moorings MW and MN were highly variable (Fig. 5). The 14-day low-passed currents were strongest in the fall and winter (Fig. 5a-d). The annual cycle of the 200–300 m vertically averaged u_a at MN had an amplitude of 0.10 m s^{-1} and explains 20% of the variance, obtained using a sinusoidal fit to daily data (not shown). These figures are similar for MW for 300-400 m averaged currents (depth ranges are chosen to ensure continuous time series, unaffected by mooring knock-downs). The cross-slope components show a less pronounced seasonality with 1-2 cm s^{-1} (5-15% variance explained) at both moorings. Temperature record at MW also shows strong seasonality. The amplitude of annual sinusoidal fit to the temperature time series, increases from 0.6°C at 200-300 m to 1°C at 500-600 m, accounting for 60-70% of the variance, and rapidly decays deeper.

The largest along-slope currents reach 0.8 m s^{-1} at both moorings, last for 1 to 2 weeks and extend as deep as 600 m. In periods with strong u_a, the cross-slope velocity is also energized. These energetic periods also correspond with the peaks in EKE$_g$ obtained from satellite altimetry at the MW location (Fig. 3c). Isotherms (available only at MW for the entire mooring record) show vertical displacements of order 100 m, consistent with mesoscale meandering of the slope current.
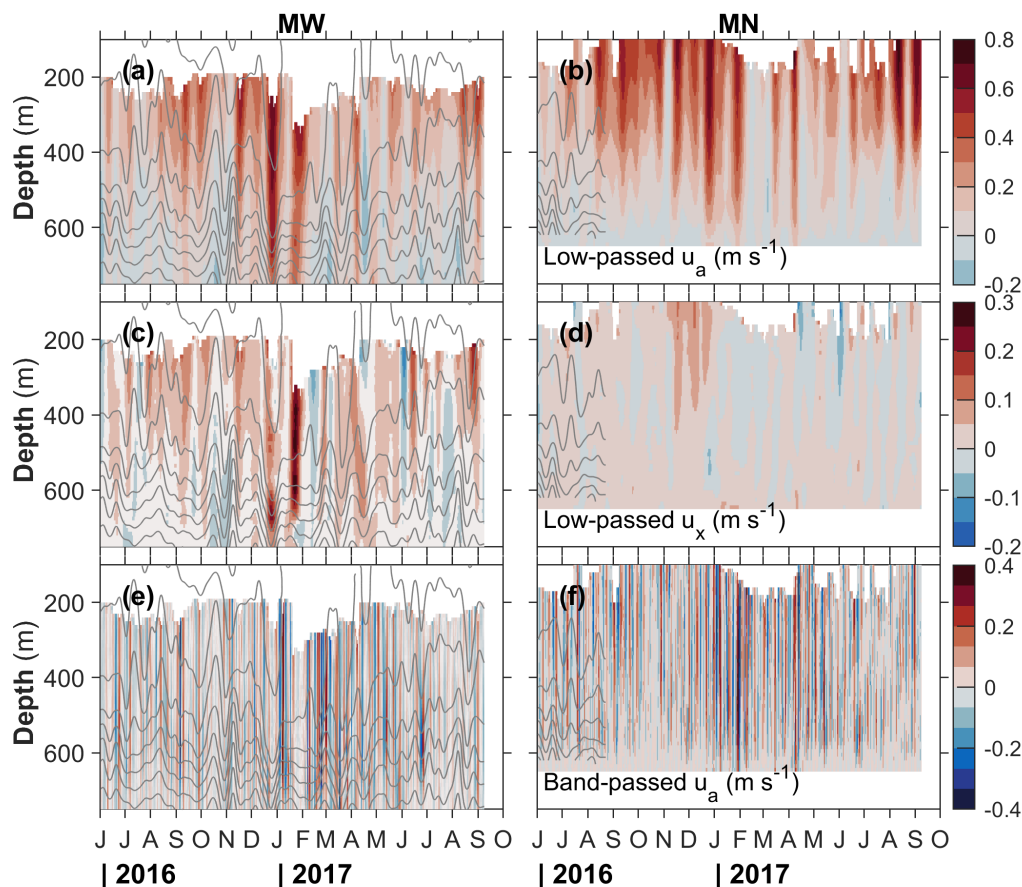
Figure 5. Depth-time variability of observed currents in the 100-700 m depth range at (left column) MW and right column (MN). The rows are (a,b) low-passed along slope current, (c,d) low-passed cross-slope current, and (e,f) band-passed along-slope current. The structure of the band-passed cross-slope (not shown) is similar with approximately half the amplitude. The variability in the deeper parts of MW is small and not shown for ease of comparison with MN. Isotherms at $1°$C intervals are shown in gray in all panels. Note the lack of water column temperature data after the first three months at MN.

150   For comparison, in the Svinøy section Skagseth and Orvik (2002) showed that the fluctuations of the slope current are a combination of longer periodic forced oscillations which are a direct response to the wind (periods in the 3–5 day and 16–32 day bands), and free waves corresponding to the first and second topographic wave modes (dominant periods of 40–70 and 80–110 h).

We analyzed fluctuations in the low-passed fields, relative to the annual cycle, to assess dominant time scales and amplitudes

155   of variability. The time series of fluctuations of u_a at MN averaged between 200–300 m shows 13 events with peak-to-peak amplitude of 0.2-0.3 m s^{-1}, with a mean duration of 8 ± 2 days, at an average interval (time separation between events) of 35 ± 10 days. Similar number of events with comparable time scale are detected for temperature oscillations exceeding $0.5°$C.

At shorter time scales, the 35 h to 14 day band-passed variability is shown in Fig. 5e-f, for u_a. The structure of band-passed u_x is very similar (not shown) with approximately half the amplitude of u_a. The band-passed fields show highly energetic
160   current variability reaching $\pm 0.4 \, \text{m s}^{-1}$ (variability for u_x is $\pm 0.2 \, \text{m s}^{-1}$). A similar event analysis of the fluctuations in the filtered band (averaged between 200–300 m at MN and 300–400 m at MW) results in very similar properties for MN and MW. Typically, 40-50 events are detected in u_a with peak-to-peak amplitude of 0.15-0.20 m s^{-1}, with a mean duration of 2 ± 1 days, at an average interval of 10 ± 7 days. The cross-slope component shows about 40 events with peak-to-peak amplitude $0.10 \pm 0.03 \, \text{m s}^{-1}$ at similar duration and time intervals. The energetics and conversion rates are further discussed in Sect. 7.
165   We estimated a de-correlation time scale as the e-folding time scale from an exponential fit to the auto-correlation function from hourly velocity time series. At both moorings at the 650-m isobath (MN and MS), 200–600 m depth-averaged along-slope currents are correlated at time scales up to 6 days. The de-correlation time scale at MW is comparable (7.3 days). For reference, advection time between the along-slope separation of the two moorings is 2 days using the mean speed of $0.15 \, \text{m s}^{-1}$. Over the 26 km separation, u_a at MN and MS are highly coherent with a maximum correlation coefficient of $r = 0.6$ at 41 h
170   lag (consistent with the 2-day advection time scale). The cross-slope components are not significantly correlated. The lateral separation between MN and MW is comparable to the Rossby deformation radius, and here u_a is highly coherent ($r = 0.9$ at 8 h lag), and the cross-slope components are fairly correlated with $r = 0.24$ at 2-day time scale with MN leading.

6   Transport

Transport calculations were made using daily-averages of the 14 day low-passed current and temperature fields from moorings
175   MW and MN, using the along-slope component of the current. Positive (northeastward, Q_p) and negative (southwestward, Q_n) transport densities (i.e. transport in a water column with 1 m width) were calculated by integrating vertically between 50 m and 650 m depth, roughly corresponding to the AW layer. Average transports over the entire record, over summer months and winter months are listed in Table 2. The net transport ($Q_p + Q_n$) was also computed in 1°C temperature classes, with the Atlantic Water transport (Q) estimated as the net transport of water warmer than 5°C. A total transport was estimated by
180   assigning a 14 km width (justified below) for each mooring. Results are summarized in Fig. 6.
The moorings are separated by approximately 6 km (horizontal distance between the locations), and when projected onto the cross-slope section to their respective isobaths, the distance is about 8 km. We assume velocity measured at each mooring is representative for the half-width (4 km) to the next mooring. We further extend the width of MW 10 km off-slope (distance to the 2500 m isobath) and MN 10 km on-shore (distance to the 250 m isobath), hence assign a 14 km effective width of
185   water column to each mooring. These choices are motivated by the coverage of the dynamic AW core at Gimsøy section (see Fig. 2). The outer edge corresponds to the location where the 5°C isotherm is shallowest, and covers the relatively steep lateral isopycnal gradient toward the slope.
The choice of a 28-km total width for the transport calculation is consistent with the lateral structure of the depth-integrated geostrophic current inferred from the Gimsøy hydrographic section. From the 4 occupations of the Gimsøy section, we cal-
190   culated the relative geostrophic transport. Depth-integrated geostrophic current peak at an isobath between 500 and 750 m,
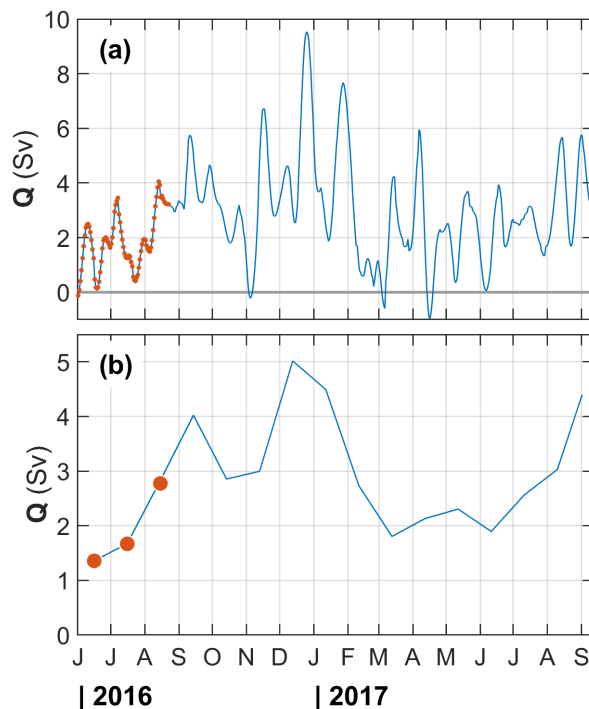
Figure 6. Total AW transport, in the 50–650 m range covered with moorings MN and MW, assigning a width of 14 km for each mooring (see text for details and sensitivity to choices). AW is defined with $\Theta > 5°C$, as measured at MW which has temperature sensors throughout the deployment. MN has temperature record in the first 3 months and the transport calculation using those records (red) agree with MW. a) Daily transports from 14 day low-passed records, b) monthly averages of the transports shown in (a).

suggesting that MN and MS are positioned near the maximum velocities of the slope current. The lateral structure of the depth-integrated relative geostrophic current was fairly symmetric and reduced to 20% of its maximum over a total width of 25–30 km. As a result we find that the choice of 28 km width for transport calculations is justified. The relative geostrophic transport for AW calculated in the Gimsøy section between 50–650 m and 50–1500 m were identical to within 0.1 Sv, hence the limited vertical range of our calculation does not introduce additional errors in the baroclinic contribution.

There is large variability in Q with 1 to 4 Sv oscillations at 2 to 4 weeks time scale (Fig. 6a). Transport maxima were observed in winter. The transport approached zero at the trough of the oscillations, but the flow reversal was negligible. Total AW transport was typically northward. Monthly averaged transport of AW increased three-fold in fall and winter with a monthly-average maximum of 5 Sv in December, from about 1.5–2 Sv in summer (Fig. 6b). The transport in temperature classes is shown in Fig. 7. When averaged over summer and winter months, separately, transport in high temperature classes (7–9°C) was stronger in winter whilst the low temperature classes (3–7°C) were stronger in summer. This is because the maximum AW-layer averaged temperatures occurred in winter (e.g., compare the winter and summer temperature profiles at MW, Fig. 4a), when the transport was also large (Fig. 6). In winter, the vertical mixing of warm surface layer resulted in a low stratified
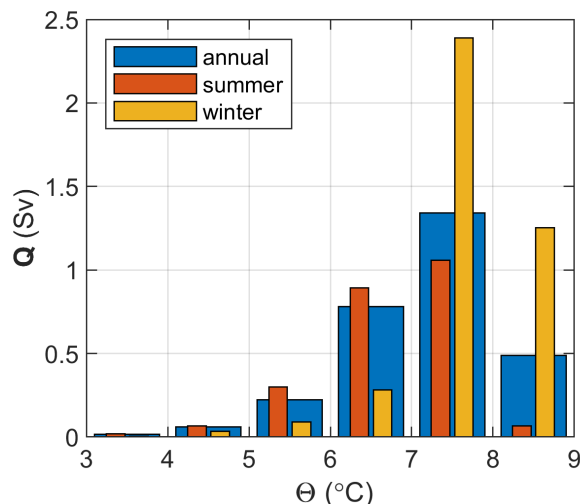
11

Ocean Science
Discussions

Open Access

EGU

Figure 7. Total transport in the 50–650 m depth range, averaged in temperature classes for the entire record (annual), summer (June, July, August) and winter (December, January, February) months.

AW layer of 7–8°C. The largest transport was in the 7–8°C water for both seasons. A seasonal variability with transport

205   and temperature maxima in winter and minima in the autumn was also observed in the Svinøy section with an annual cycle amplitude in currents of about $0.10\,\mathrm{m\,s^{-1}}$ (Orvik and Skagseth, 2005).

Two moorings closely spaced over the slope cannot capture the full dynamics of the slope boundary current. However, as described above, the CTD sections collected at different months along the standard Gimsøy Section, in close vicinity of the moorings, suggest that the mean slope of the isopycnals can be approximated from the mooring records. The sections also

210   suggest that the bulk of the AW is in the upper 650 m, which is resolved by our moorings.

AW transports are not sensitive to the definition of the AW temperature and vertical integration limits; however, the crude estimate of the width of the slope current must be treated with caution. Recalculating the transport using water with $T \geq 3$ (instead of $T \geq 5$) increases Q by 0.1 Sv. Including the top 50 m increases the total mean transport by 0.4 Sv (from 2.8 Sv).

Table 2. Volume transport calculations. Q_N is directed northwest out of section, Q_S is southeastward, and Q is the total AW transport with $\Theta \geq 5°\mathrm{C}$

Period	Transport (Sv)		
	Q_p	Q_n	Q
Annual	3.0 $\pm$1.8	-0.1 $\pm$0.2	2.8 $\pm$1.8
Summer	2.5 $\pm$1.3	-0.1 $\pm$0.1	2.3 $\pm$1.2
Winter	4.1 $\pm$2.5	0.0 $\pm$0.1	4.0 $\pm$2.5

The sensitivity to the choice of mooring width is approximately linear. A total current width of 10 km (i.e. assigning 5 km to

215   each mooring instead of 14 km) reduces the mean transport from 2.8 to 1 Sv.

7   Energetics

The kinetic energy content and variability of the slope current, and conversion rates associated with barotropic and baroclinic

instability of the current are presently unconstrained by observations. Using our limited mooring records, we attempt to quantify

the energetics of the slope current at the Lofoten Escarpment. For the following analysis, we obtained the fluctuations, denoted

220   by primes, by band-pass filtering the hourly data with cutoff frequencies corresponding to 14 day and 35 hours.

We start with the variability in depth-averaged along and cross slope currents, the horizontal eddy kinetic energy density,

EKE, and their relation to wind forcing. The EKE in units of $\mathrm{J\,kg^{-1}}$ or $\mathrm{m^2\,s^{-2}}$, is

$$\mathrm{EKE} = \frac{1}{2}\left(u'^2 + v'^2\right) . \tag{1}$$

The along-slope current variability and the evolution of EKE were partly forced by the along-slope wind modulating the

225   geostrophic shear by cross-front Ekman transport (Fig. 8a-c). The annual average wind speed (4.3 ± 2.3 m s^{-1}), increased

to 6 m s^{-1} in winter with a maximum of 11 m s^{-1}. Depth averaged (200–600 m) u_a at MW was 0.15 ± 0.12 m s^{-1} with a

maximum of 0.6 m s^{-1} in winter (winter average was 0.25 ± 0.16 m s^{-1}). The maximum correlation between depth-averaged

u_a and the along-slope component of the wind W_a was obtained at 2 day lag (r=0.6). While no significant correlation was

detected with the cross-slope component, u_x increased in amplitude and variability in winter (from its annual average of 0.03

230   $\pm$ 0.04 m s^{-1}) to 0.05 ± 0.07 m s^{-1} reaching a maximum of 0.26 m s^{-1}.

From 30-day moving averages, EKE was $(65 \pm 38) \times 10^{-4}$ with a maximum of 185×10^{-4} m^2 s^{-2}. Daily average values

were similar, but with 3 times larger standard deviation and a maximum of 790×10^{-4} m^2 s^{-2}. The maximum EKE was

observed in winter, consistent with stronger and favorable downfront winds. When averaged over winter months EKE was

$(100 \pm 41) \times 10^{-4}$ m^2 s^{-2}.

235   An estimate of the baroclinic (BC) and barotropic (BT) conversion rates can be made assuming no variability in the along-

slope direction and the cross-slope gradients dominate. Similar calculations were made both in idealized (channel) model

studies (e.g., Spall et al., 2008) and limited mooring data (e.g., in the West Spitsbergen Current, von Appen et al., 2016; Håvik

et al., 2017, in the East Greenland Current). A positive value of BC indicates conversion from mean potential energy into EKE,

by growing eddies extracting energy from the mean state. The conversion from mean kinetic energy into EKE is quantified by

240   BT. In this case, the kinetic energy is extracted from the mean flow by eddies transporting along-slope momentum down the

mean velocity gradient. The baroclinic conversion rate can be approximated by

$$\mathrm{BC} = g\overline{v'\rho'}\frac{\partial z}{\partial y} , \tag{2}$$
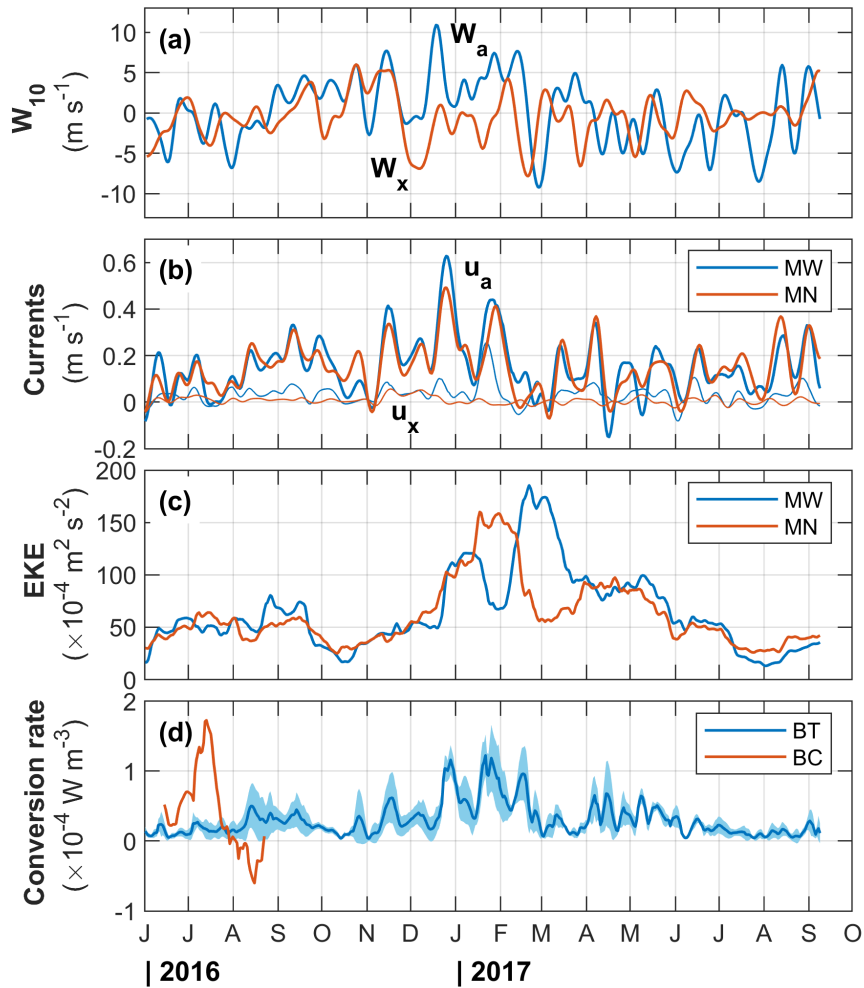
Ocean Science
Discussions

Figure 8. Time series of a) ERA5 wind along-slope (W_a) and cross-slope (W_x) components, b) 200–600 m averaged u_a and u_x measured at mooring MW (blue) and MN (red), c) 200–600 m averaged EKE at MW (blue) and MN (red) and d) barotropic (BT, blue) and baroclinic (BC, red) conversion rates. BC is at 400 m level and only available for 3 months. BT is the depth-average and one standard deviation envelope over calculations at 200, 300, 400, 500 and 600 m. All curves are 30-day moving averages.

ρ_0 is a reference density, and g is gravitational acceleration, and an overbar denotes temporal averaging. We used CHECK! NOT 1 MONTH? 14 day moving averaging. The mean isopycnal slope, $\partial z/\partial y$, was calculated as $\partial \overline{\rho}/\partial y / \partial \overline{\rho}/\partial z$. The barotropic conversion rate can be approximated by

$$\mathrm{BT} = -\rho_0 \overline{u'v'} \frac{\partial \overline{u}}{\partial y} \; . \tag{3}$$

The 8-km cross-slope separation of the moorings may be too small to characterize the lateral shear, and the resulting BT can be an underestimate. To derive an upper limit, and likely closer to a more realistic value for BT, we assume that $\overline{u}$ decreases from the largest value of the observation at MW and MN to 0 over a decay length scale of 15 km, and use the largest of the
250 Reynolds stress $(\overline{u'v'})$ from the two moorings.

While the velocity data coverage is good in both moorings, density (through salinity measurement) measurements are limited. At MW, density measurements are available at target depths of 75, 380, 980 and 1476 m. At MN, the near-bottom sensor (648 m) recorded throughout, but the sensors at 165 and 455 m recorded only until September (the water column line was cut 3 months after the deployment). Note that motion-corrected mooring data were gridded and interpolated. Based on the density
255 measurement coverage, we picked the 400-m level as a representative depth (in AW and in the wedge of AW current with steep isopycnals, Fig. 2) where we can obtain vertical and lateral gradients, but only for 3 months into the record. We obtained the vertical gradient at 400 m at MW using the records at 300 and 500 m. We obtained the lateral gradient from the records at 400 m. Final conversion rates were obtained by moving averaging over 30 days. Whilst the baroclinic conversion rate time series is limited only to three months, the barotropic conversion rate can be calculated for the entire duration. We computed BT at 300,
260 400, 500 and 600 m depths. Results are summarized in Fig. 8d. The conversion rates calculated from two moorings may not be representative of the volume-averaged conversion rates over the slope region and must be interpreted with caution. This is discussed in detail in the Appendix, using high-resolution numerical model fields.

Average barotropic conversion rate (averaged over both moorings, over multiple levels and over 14 months) was $(0.3 \pm 0.2) \times 10^{-4}$ W m^{-3}. Maximum value reached 1.2×10^{-4} W m^{-3}. The baroclinic conversion rate (only available in the summer for
265 the first three months of the mooring period) was comparable, $(0.4 \pm 0.6) \times 10^{-4}$ with a maximum of 1.7×10^{-4} W m^{-3}

Observed EKE and the conversion rates at the Lofoten Escarpment can be compared to other relevant observations. In Fram Strait von Appen et al. (2016) analyzed 12 year long time series from moorings with focus on the West Spitsbergen Current. EKE at 75 m depth was 50×10^{-4} m^2 s^{-2} in summer, and increased to 200×10^{-4} m^2 s^{-2} in winter. At 250 m depth the magnitude was approximately reduced to half. These values, overall, are similar to the EKE at the Lofoten slope. Conversion
270 rates at WSC were also comparable: BT was on the order 0.1×10^{-4} W m^{-3}, and BC at 75 m was 0.5×10^{-4} W m^{-3} in summer, increasing to 1.5×10^{-4} W m^{-3} in winter. Summer mean and maximum values are identical (within measurement uncertainties) to the corresponding values from our observations at 400 m in summer.

Using a mooring array Håvik et al. (2017) analyzed the structure and variability of the shelfbreak East Greenland Current, for the period September 2011 to August 2012. EKE at 100 m was up to 700×10^{-4} m^2 s^{-2} in November 2011 when a reversal
275 of shelf break current was observed, otherwise typical values varied between 10×10^{-4} and 100×10^{-4} m^2 s^{-2}, similar to the values at the Lofoten Escarpment. Ignoring the energetic reversal event, BT at 100 m was on the order 0.1×10^{-4} W m^{-3}, similar to the WSC and the slope current, and BC varied in the range of $(1-5) \times 10^{-4}$ W m^{-3}.

The conversion rates calculated from our moorings may not be representative of the volume-averaged conversion rates over the slope region. Computations from the high-resolution numerical model fields (Appendix A) show that the calculations from
280 two moorings overestimate BT and underestimate BC (Fig. A2). Volume averaging over the highly variable spatial structure of BT with changing signs lead to negligible BT, which cannot be resolved with the moorings. BC on the other hand, dominates

with values in the range of $(1-2) \times 10^{-4} \, \mathrm{W\,m^{-3}}$, and cannot be captured by the calculations from a single level at 400 m depth. Based on this discussion, we propose that the conversion rates on the Lofoten Escarpment are likely dominated by baroclinic instability of the slope current.

285 ## 8 Conclusions

The Norwegian Atlantic Slope Current at the Lofoten Escarpment is described using 14-month long mooring records in the period from June 2016 to September 2017. Despite the limited number of moorings, the observations resolve the core of the current from 200 to 650 m depth over the shelf break and the upper continental slope. The data set is the first moored observations on yearly time scale from this region, and offers important constraints on mean properties, transport rates, temporal
290 variability, and energy conversion rates of the slope current.

Temporal average of the 200–600 m averaged current is $0.15 \, \mathrm{m\,s^{-1}}$ with an annual cycle amplitude of $0.1 \, \mathrm{m\,s^{-1}}$ and strongest currents in winter. 14-day low pass filtered along-slope currents reach $0.8 \, \mathrm{m\,s^{-1}}$, lasting for 1 to 2 weeks and extend as deep as 600 m. The variability in the along-slope current is partly forced by the along-slope wind stress, with a maximum correlation of 0.6 at 2 day lag. In contrast to observations in Svinøy, the slope current is not barotropic and varies strongly with depth
295 (shear of 0.05 to $0.1 \, \mathrm{m\,s^{-1}}$ per 100 m in all seasons).

The average volume transport is 2.8 ± 1.8 Sv, with summer and winter averages of 2.3 and 4.0 Sv, respectively. The largest transport is associated with warm water in all seasons, and the water temperatures are the highest in winter.

Calculations of the barotropic and baroclinic conversion rates using the moorings are supplemented by high resolution numerical model. While the conversion from mean kinetic energy into eddy energy (e.g. barotropic instability) is likely negligible
300 over the Lofoten Escarpment, the baroclinic conversion from mean potential energy into eddy kinetic energy (e.g. baroclinic instability), can be substantial with volume-averaged values on the order of $10^{-4} \, \mathrm{W\,m^{-3}}$. Eddy kinetic energy and conversion rates in the slope current are comparable to the published results from the West Spitsbergen Current and the East Greenland Current.

Fishing activity in the region makes it highly challenging to maintain moorings; however, extended time series with better
305 cross-slope and vertical coverage are needed to study the dynamics and variability of the slope current. The attempts to calculate (observation-based) energy conversion rates remain inconclusive. Utilization of autonomous underwater vehicles, such as gliders, can help collecting high quality observations, but will be difficult to operate in the strong boundary current. The slope current and its instability is an important player in the energetics of the Lofoten Basin and merits further studies.

Appendix A: Conversion rates from a high resolution model

Barotropic and baroclinic conversion rates calculated from moorings may not be representative of the volume-averaged conversion rates in the region. In order to assess how representative they are and to better interpret the results, we perform similar calculations using outputs from a high-resolution Regional Ocean Modelling System (ROMS) configuration in the Nordic Seas,

315 and compare these to full resolution and volume-averaged calculations. ROMS is a hydrostatic model with terrain-following coordinates that solves the primitive equations on a staggered C-grid (Shchepetkin and McWilliams, 2009; Haidvogel et al., 2008). The model fields used here have a horizontal resolution of 800 m, 60 vertical layers with increased resolution towards the surface (1-3 m at the surface, about 60 m at the bottom) and are stored as 6 hourly outputs. The model fields are used and described in detail in Dugstad et al. (2019b).

320 We first compute the baroclinic and barotropic conversion rates over a domain covering the slope region identified in Fig. A1. The conversion rates in a 3D, right-handed coordinate system are given in Olbers et al. (2012, , pp.376-377). The baroclinic conversion rates are computed from

$$\mathrm{BC} = -\rho_0 \overline{\mathbf{u}'_h b'} \cdot \nabla_h \bar{b}/N^2 = \rho_0 g \left(\frac{\partial \overline{\rho}}{\partial z}\right)^{-1} \left(\overline{u'\rho'}\frac{\partial \overline{\rho}}{\partial x} + \overline{v'\rho'}\frac{\partial \overline{\rho}}{\partial y}\right). \tag{A1}$$

Here $\mathbf{u}_h = (u,v)$ denotes the horizontal velocity field with the components pointing in the x- and y-direction on the model

325 grid, $b = \frac{-g\rho}{\rho_0}$ is the buoyancy, $N^2 = -\frac{g}{\rho_0}\frac{\partial \overline{\rho}}{\partial z}$ is the buoyancy frequency, ρ the potential density referenced to surface, g the gravitational acceleration, and $\rho_0 = 1027 \, \mathrm{kg\,m^{-3}}$ is a reference density. The primes denote deviations from an average state (overbar), averaged over multiple eddy time scales, e.g. for velocity $u' = u - \overline{u}$. In this coordinate system, a positive value of BC indicates a transfer of potential energy from the mean flow to eddies.

We calculate the barotropic conversion rates from

330 $$\mathrm{BT} = -\rho_0 \overline{u'\mathbf{u}'} \cdot \nabla \overline{u} - \overline{v'\mathbf{u}} \cdot \nabla \overline{v} = -\rho_0 \left(\overline{u'u'}\frac{\partial \overline{u}}{\partial x} + \overline{u'v'}\left(\frac{\partial \overline{u}}{\partial y} + \frac{\partial \overline{v}}{\partial x}\right) + \overline{v'v'}\frac{\partial \overline{v}}{\partial y}\right). \tag{A2}$$

A positive value of BT indicates a transfer of kinetic energy from the mean flow to eddies.

We compute BC and BT after interpolating the model fields to uniform z-levels of 10 m vertical spacing. The time averaging and fluctuations are calculated over monthly windows to avoid any seasonal bias. We arbitrarily chose the year 1999 from the model fields (available from 1996 to the end of 1999). Monthly conversion rates are then averaged vertically between 100-1000

335 m depth (i.e., we exclude the near-surface variability). A global annual average is then obtained by averaging over these 12 months. Results are shown in Fig. A1.

The baroclinic conversion rates are typically positive and largest along the slope, indicating that potential energy is extracted from the slope current to feed eddies that are generated there. The barotropic conversion rates, on the other hand, show larger spatial variability. The magnitudes are smaller and the sign often changes. The baroclinic processes therefore appear to be the

340 main contributor to the conversion of energy from the mean flow to eddies along the slope.
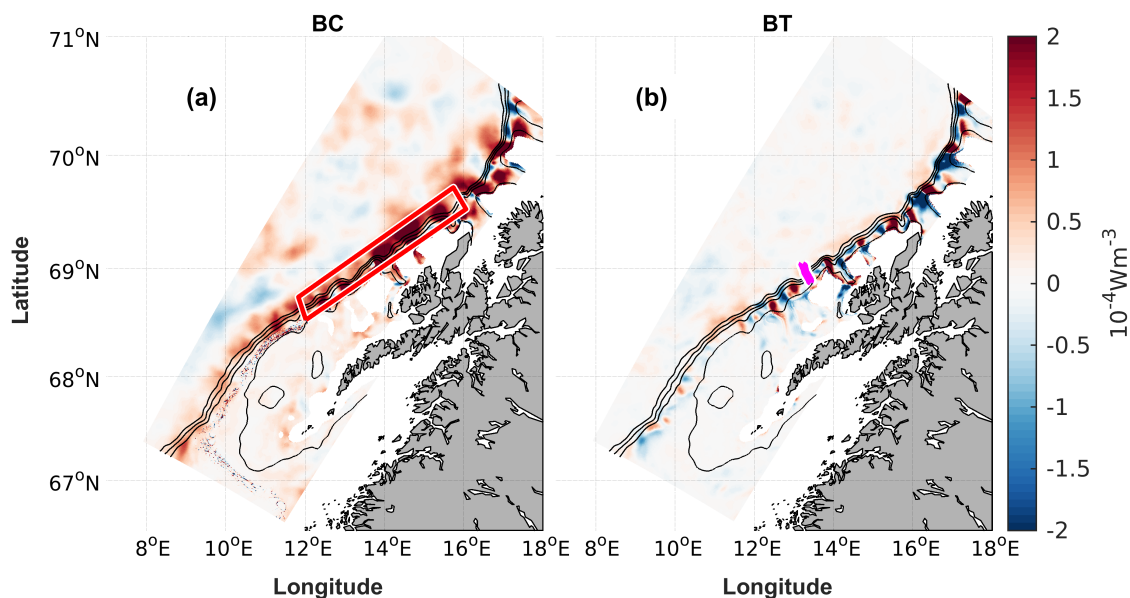
Figure A1. Maps of (a) baroclinic and (b) barotropic conversion rates averaged over one year (1999) and between 100-1000 m depth or to bottom in shallower areas. The red box in (a) is the slope region where volume-averaged conversion rates are computed, see Fig A2a. The magenta line across the slope in (b) marks a segment across the mooring positions used for comparison of volume averaged and segment/virtual mooring calculations (see text and Fig A2b).

Monthly conversion rates over the slope, volume averaged over the red box identified in Fig A1a and between 100 and 1000 m depth show that the baroclinic conversion rates dominate (Fig A2a), implying the baroclinic instability of the slope current extracts energy from the mean flow to eddies.

The motivation here is to assess whether the conversion rates obtained from a mooring array are representative of the volume-
345   averaged values. To do this we define a segment across the slope (magenta in Fig A1b), that stretches between the mooring positions of MW and MN and extend further by 10 km at both sides. We then perform two types of calculations: we compute BT and BC at the model grid resolution and average along the entire segment, and we compute BT and BC using model data from the virtual mooring positions. To be consistent with the observations we apply Equation 2 and 3 and rotate the coordinate system to along and across isobaths. To directly compare with the mooring analysis, we perform baroclinic conversion rates
350   only at 400 m depth while the barotropic computations are performed as an average between 200-600 m. The motivation of performing the segment calculation is to better resolve the lateral shear compared to only two virtual moorings. Calculations along the segment are based on about 40 grid points, hence are a more robust estimate. The conversion rates are shown in Fig A2b.

While there are differences between the segment (solid lines) and virtual mooring (dashed lines) estimates, the conversion
355   rates are comparable with no systematic differences. Lateral shear and isopycnal slopes using only two moorings separated by
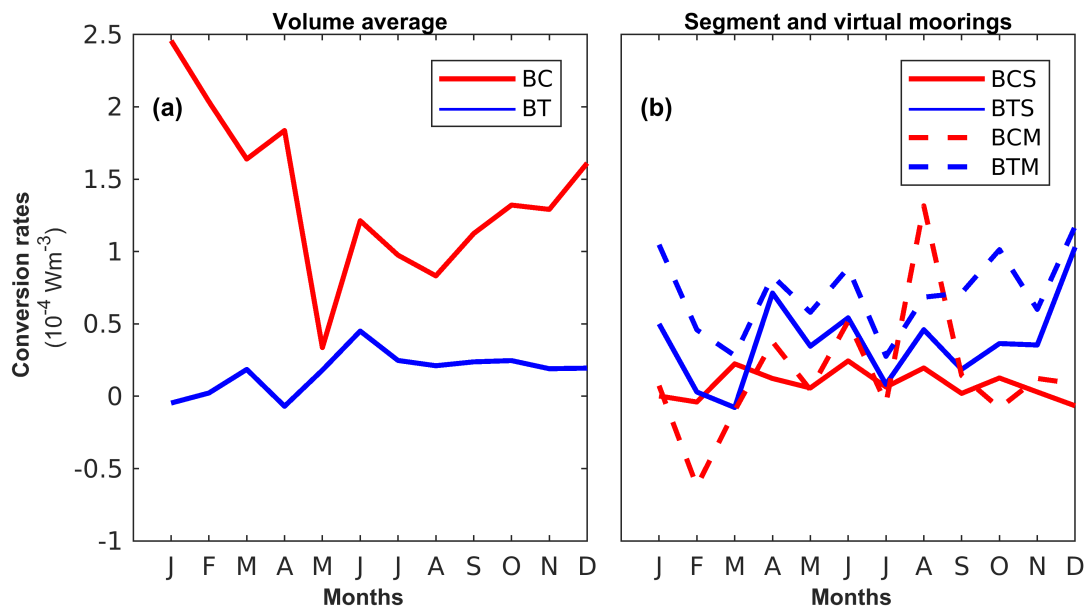
Figure A2. (a): Monthly-averaged baroclinic (red) and barotropic (blue) conversion rates, vertically averaged between 100 and 1000 m depth and inside the red box in Fig A1a. Calculations were made using Equations A1 and A2. (b): Monthly-averaged baroclinic (red) and barotropic (blue) conversion rates averaged along the magenta segment in Fig A1b (solid lines) and between mooring stations MN and MW similar to the observations (dashed lines). The calculations are based on Equation 2 and 3, similar to the observations. The coordinate system is also rotated accordingly. The baroclinic conversion rates are shown at 400 m depth, while the barotropic conversion rates are shown as an average between 200-600 m depth.

about 8 km could thus be used in calculations of the conversion rates in one transect. We also note that the BT is similar to the observations (blue line in Fig 8 d) with magnitudes between $(0-1) \times 10^{-4}$W m^{-3} and maximum values around 1×10^{-4}W m^{-3}. Observed BC is available only in the summer months (red line in Fig 8 d), and compare fairly well with the BC from the virtual moorings. However, a comparison with the volume-averaged conversion rates shows that calculations using virtual moorings

360 overestimate BT, underestimate BC, introduce spurious changes in sign, and are not representative of the overall conversion rates on the slope. The discrepancy in BT is partly due to the different depth-averaging (100-1000 m vs 200-600 m, note the latter range is constrained by available observations whereas the former covers the depth range of interest on the slope region, excluding the upper surface processes) , and partly because the volume-averaged calculations include the divergent terms (first and last term in Equation A2) in addition to the terms related to shear (second term). We notice that the divergent

365 terms often occur with opposite signs (not shown) and therefore to some extent cancel out the contribution from the terms related to shear. Also note that the highly variable spatial structure observed in BT cannot be resolved with a single segment. The discrepancy in BC is mainly because the volume-averaged calculations are based on a depth average between 100-1000 m, whereas the mooring calculations are only taken at 400 m depth due to limited observations. We therefore conclude that the

Ocean Science
Discussions

370   mooring-derived conversion rates must be interpreted with caution and may not be representative of the real conversion rates
in the region.

Ocean Science
Discussions

Open Access

EGU

References

Andersson, M., Orvik, K. A., LaCasce, J. H., Koszalka, I., and Mauritzen, C.: Variability of the Norwegian Atlantic Current and associated eddy field from surface drifters, J. Geophys. Res., 116, C08032, https://doi.org/10.1029/2011jc007078, 2011.

Bosse, A. and Fer, I.: Mean Structure and Seasonality of the Norwegian Atlantic Front Current Along the Mohn Ridge From Repeated Glider
385   Transects, Geophys. Res. Lett, 46, 13 170–13 179, https://doi.org/10.1029/2019GL084723, 2019.

Bosse, A., Fer, I., Søiland, H., and Rossby, T.: Atlantic Water Transformation Along Its Poleward Pathway Across the Nordic Seas, J. Geophys. Res., 123, 6428–6448, https://doi.org/10.1029/2018JC014147, 2018.

Bosse, A., Fer, I., Lilly, J., and Søiland, H.: Dynamical controls on the longevity of a non-linear vortex: The case of the Lofoten Basin Eddy, Scientific Reports, 9, 13 448, https://doi.org/10.1038/s41598-019-49599-8, 2019.

390 C3S: ERA5: Fifth generation of ECMWF atmospheric reanalyses of the global climate, Copernicus Climate Change Service Climate Data Store (CDS), https://cds.climate.copernicus.eu/cdsapp#!/home, 2017.

Dee, D. P., Uppala, S. M., Simmons, A. J., Berrisford, P., Poli, P., Kobayashi, S., Andrae, U., Balmaseda, M. A., Balsamo, G., Bauer, P., Bechtold, P., Beljaars, A. C., van de Berg, L., Bidlot, J., Bormann, N., Delsol, C., Dragani, R., Fuentes, M., Geer, A. J., Haim-berger, L., Healy, S. B., Hersbach, H., Hólm, E. V., Isaksen, L., Kållberg, P., Köhler, M., Matricardi, M., Mcnally, A. P., Monge-Sanz,
395   B. M., Morcrette, J. J., Park, B. K., Peubey, C., de Rosnay, P., Tavolato, C., Thépaut, J. N., and Vitart, F.: The ERA-Interim reanalysis: Configuration and performance of the data assimilation system, Quarterly Journal of the Royal Meteorological Society, 137, 553–597, https://doi.org/10.1002/qj.828, 2011.

Dugstad, J., Fer, I., LaCasce, J., Sanchez de La Lama, M., and Trodahl, M.: Lateral Heat Transport in the Lofoten Basin: Near-Surface Pathways and Subsurface Exchange, J. Geophys. Res., 124, https://doi.org/10.1029/2018jc014774, 2019a.

400 Dugstad, J. S., Koszalka, I. M., Isachsen, P. E., Dagestad, K.-F., and Fer, I.: Vertical Structure and Seasonal Variability of the Inflow to the Lofoten Basin Inferred From High-Resolution Lagrangian Simulations, J. Geophys. Res., 124, https://doi.org/10.1029/2019jc015474, 2019b.

Fer, I.: Measurements of currents, temperature and salinity from moorings in the Lofoten Basin, Norwegian Sea: June 2016 September 2017, 2020.

405 Fer, I., Bosse, A., Ferron, B., and Bouruet-Aubertot, P.: The dissipation of kinetic energy in the Lofoten Basin Eddy, J. Phys. Oceanogr., 48, 1299–1316, https://doi.org/10.1175/JPO-D-17-0244.1, 2018.

Haidvogel, D. B., Arango, H., Budgell, W. P., Cornuelle, B. D., Curchitser, E., Di Lorenzo, E., Fennel, K., Geyer, W. R., Hermann, A. J., Lanerolle, L., Levin, J., McWilliams, J. C., Miller, A. J., Moore, A. M., Powell, T. M., Shchepetkin, A. F., Sherwood, C. R., Signell, R. P., Warner, J. C., and Wilkin, J.: Ocean forecasting in terrain-following coordinates: Formulation and skill assessment of the Regional Ocean
410   Modeling System, Journal of Computational Physics, 227, 3595–3624, https://doi.org/https://doi.org/10.1016/j.jcp.2007.06.016, 2008.

Håvik, L., Våge, K., Pickart, R. S., Harden, B., Appen, W.-J. v., Jonsson, S., and Østerhus, S.: Structure and Variability of the Shelfbreak East Greenland Current North of Denmark Strait, J. Phys. Oceanogr., 47, 2631–2646, https://doi.org/10.1175/jpo-d-17-0062.1, 2017.

Høydalsvik, F., Mauritzen, C., Orvik, K. A., LaCasce, J. H., Lee, C. M., and Gobat, J.: Transport estimates of the Western Branch of the Norwegian Atlantic Current from glider surveys, Deep-Sea Res. I, 79, 86–95, https://doi.org/10.1016/j.dsr.2013.05.005, 2013.

415 Isachsen, P. E.: Baroclinic instability and the mesoscale eddy field around the Lofoten Basin, J. Geophys. Res., 120, 2884–2903, https://doi.org/10.1002/2014JC010448, 2015.

Ocean Science
Discussions

Isachsen, P. E., Koszalka, I., and LaCasce, J. H.: Observed and modeled surface eddy heat fluxes in the eastern Nordic Seas, J. Geophys. Res., 117, C08020, https://doi.org/10.1029/2012JC007935, 2012.

Ivanov, V. and Korablev, A. A.: Formation and regeneration of the pycnocline lens in the Norwegian Sea, Russ. Meteor. Hydrol., 9, 62–69, 1995.

Köhl, A.: Generation and stability of a quasi-permanent vortex in the Lofoten Basin, J. Phys. Oceanogr., 37, 2637–2651, https://doi.org/10.1175/2007JPO3694.1, 2007.

Olbers, D., Willebrand, J., and Eden, C.: Ocean Dynamics, Springer Verlag Berlin, Berlin, 2012.

Orvik, K. A. and Niiler, P.: Major pathways of Atlantic water in the northern North Atlantic and Nordic Seas toward Arctic, Geophys. Res. Lett., 29, https://doi.org/10.1029/2002GL015002, 2002.

Orvik, K. A. and Skagseth, O.: Monitoring the Norwegian Atlantic slope current using a single moored current meter, Cont. Shelf Res., 23, 159–176, https://doi.org/10.1016/S0278-4343(02)00172-3, 2003.

Orvik, K. A. and Skagseth, O.: Heat flux variations in the eastern Norwegian Atlantic Current toward the Arctic from moored instruments, 19952005, Geophys. Res. Lett., 32, https://doi.org/10.1029/2005gl023487, 2005.

Orvik, K. A., Skagseth, , and Mork, M.: Atlantic inflow to the Nordic Seas: current structure and volume fluxes from moored current meters, VM-ADCP and SeaSoar-CTD observations, 19951999, Deep-Sea Res. I, 48, 937–957, https://doi.org/10.1016/S0967-0637(00)00038-8, 2001.

Rhines, P., Häkkinen, S., and Josey, S. A.: Is Oceanic Heat Transport Significant in the Climate System?, in: ArcticSubarctic Ocean Fluxes: Defining the Role of the Northern Seas in Climate, edited by Dickson, R. R., Meincke, J., and Rhines, P., pp. 87–109, Springer Netherlands, Dordrecht, 2008.

Rossby, T., Ozhigin, V., Ivshin, V., and Bacon, S.: An isopycnal view of the Nordic Seas hydrography with focus on properties of the Lofoten Basin, Deep-Sea Res. I, 56, 1955–1971, https://doi.org/https://doi.org/10.1016/j.dsr.2009.07.005, 2009a.

Rossby, T., Prater, M. D., and Søiland, H.: Pathways of inflow and dispersion of warm waters in the Nordic seas, J. Geophys. Res., 114, C04011, https://doi.org/10.1029/2008JC005073, 2009b.

Seager, R., Battisti, D. S., Yin, J., Gordon, N., Naik, N., Clement, A. C., and Cane, M. A.: Is the Gulf Stream responsible for Europe's mild winters?, Quart. J. Roy. Meteor. Soc., 128, 2563–2586, https://doi.org/10.1256/qj.01.128, 2002.

Shchepetkin, A. F. and McWilliams, J. C.: Correction and commentary for Ocean forecasting in terrain-following coordinates: Formulation and skill assessment of the regional ocean modeling system by Haidvogel et al., J. Comp. Phys. 227, pp. 35953624, Journal of Computational Physics, 228, 8985–9000, https://doi.org/https://doi.org/10.1016/j.jcp.2009.09.002, 2009.

Skagseth, O. and Orvik, K. A.: Identifying fluctuations in the Norwegian Atlantic Slope Current by means of empirical orthogonal functions, Cont. Shelf Res., 22, 547–563, https://doi.org/10.1016/S0278-4343(01)00086-3, 2002.

Søiland, H. and Rossby, T.: On the structure of the Lofoten Basin Eddy, J. Geophys. Res., 118, 4201–4212, https://doi.org/10.1002/jgrc.20301, 2013.

Spall, M. A.: Dynamics of Downwelling in an Eddy-Resolving Convective Basin, J. Phys. Oceanogr., 40, 2341–2347, https://doi.org/10.1175/2010jpo4465.1, 2010.

Spall, M. A., Pickart, R. S., Fratantoni, P. S., and Plueddemann, A. J.: Western Arctic Shelfbreak Eddies: Formation and Transport, J. Phys. Oceanogr., 38, 1644–1668, https://doi.org/https://doi.org/10.1175/2007jpo3829.1, 2008.

Sundby, S.: Recruitment of Atlantic cod stocks in relation to temperature and advectlon of copepod populations, Sarsia, 85, 277–298, https://doi.org/10.1080/00364827.2000.10414580, 2000.

Ocean Science
Discussions

Open Access

EGU

455 Volkov, D. L., Kubryakov, A. A., and Lumpkin, R.: Formation and variability of the Lofoten basin vortex in a high-resolution ocean model, Deep-Sea Res. I, 105, 142–157, https://doi.org/10.1016/j.dsr.2015.09.001, 2015.

von Appen, W.-J., Schauer, U., Hattermann, T., and Beszczynska-Möller, A.: Seasonal Cycle of Mesoscale Instability of the West Spitsbergen Current, J. Phys. Oceanogr., 46, 1231–1254, https://doi.org/10.1175/jpo-d-15-0184.1, 2016.